Submitted to *Crystals*. Pages 1 - 18.

crystals
ISSN 2073-4352
www.mdpi.com/journal/crystals

Review

The origin of Raman D Band: Bonding and Antibonding Orbitals in Graphene

Ken-ichi Sasaki [1,⋆], **Yasuhiro Tokura** [1,2], **and Tetsuomi Sogawa** [1]

[1] NTT Basic Research Laboratories, Nippon Telegraph and Telephone Corporation, 3-1 Morinosato Wakamiya, Atsugi, Kanagawa 243-0198, Japan

[2] Graduate School of Pure and Applied Sciences, University of Tsukuba, Tsukuba, Ibaraki 305-8571, Japan

***** Author to whom correspondence should be addressed; sasaki.kenichi@lab.ntt.co.jp

Version November 22, 2012 submitted to Crystals. *Typeset by LaTeX using class file mdpi.cls*

Abstract: In Raman spectroscopy of graphite and graphene, the D band at $\sim 1355\text{cm}^{-1}$ is used as the indication of the dirtiness of a sample. However, our analysis suggests that the physics behind the D band is closely related to a very clear idea for describing a molecule, namely bonding and antibonding orbitals in graphene. In this paper, we review our recent work on the mechanism for activating the D band at a graphene edge.

Keywords: Graphene; Edge; Raman D Band; Molecular Orbitals

1. Introduction

Bonding and antibonding orbitals are basic ideas for describing molecules. Bonding orbitals contribute to the formation of a molecule, whereas antibonding orbitals weaken the bonding and destabilize a molecule. Normally, bonding orbitals are more stable than antibonding orbitals in terms of energy and thus a molecule is stable unless sufficient electrons occupy the antibonding orbitals.

Graphene [1,2] is unique with respect to its molecular orbitals. The bonding and antibonding orbitals in graphene are degenerate, and various types of linear combination of these orbitals form the Fermi surface expressed by the isoenergy sections of Dirac cones. This degeneracy plays an essential role in various phenomena. For example, graphene is stable with respect to a large shift of the Fermi energy position [3]. Another notable example is that graphene exhibits high mobility. Elastic backward scattering between the bonding and antibonding orbitals induced by long-range impurity potential is

suppressed because they are orthogonal [4]. In this paper, we show that the bonding and antibonding orbitals in graphene are key factors in the activation mechanism of the D band observed at a graphene edge.

Since the discovery of the D band, much interest has focused on its origin. Tuinstra and Koenig attributed the D band to an A_{1g} zone-boundary mode at the edge of a sample (see Fig. 1) on the grounds that the Raman intensity is proportional to the edge percentage and that the edge causes a relaxation of the momentum conservation needed for activating a zone-boundary phonon [5]. Katagiri et al. confirmed that the D band originates from an edge (or discontinuity in the carbon network) by observing the light polarization dependence of the D band intensity at graphite edge planes [6]. The atomic arrangement of an edge has two principal axes; armchair and zigzag edges. Cançado et al. showed that the armchair (zigzag) edge is relevant (irrelevant) to the relaxation of the momentum conservation for a zone-boundary phonon [7]. In addition, they found that the D band Raman intensity depends on the polarization of laser light, that is, the intensity is maximum (minimum) when the polarization is parallel (perpendicular) to the armchair edge. The light polarization dependence of the D band is also observed ubiquitously at the armchair edges of a single layer of graphene, which suggests that out-of-plane coupling in graphite is not essential to the origin of the D band [8–10].

A model of the D band must at least explain the observed properties: (i) the D band intensity increases only at an armchair edge, and (ii) the D band intensity is dependent on the laser light polarization.

The current D band model is a double resonance model [11]. In this model, a photo-excited electron passes through two resonance states, which enhances the Raman intensity of a phonon with nonzero wave vector $\mathbf{q} \neq 0$. This model is not concerned with the details of electron-phonon and electron-light matrix elements, and it does not provide clear explanations of the properties of the D band. Also, the intensity calculated with this model is dependent on the lifetime of the resonance states. Usually, the lifetime is determined in such a manner that a calculated result reproduces experimental data. In this sense, the double resonance model is phenomenological. Because the lifetime is shorter in a defective graphene sample, double resonance does not necessarily mean an enhancement of the D band Raman intensity. On the other hand, the model can account for the so-called dispersive behavior of the D band [11]. However, as we will show in this paper, dispersive behavior is characteristic of A_{1g} modes, rather than an inherent property of the D band. In fact, dispersive behavior is observed also for the $2D$ band, and the excitation does not need an edge, which is in contrast to the D band.

In this paper we show that the observed properties of the D band are naturally explained in terms of simple ideas based on molecular orbitals and momentum conservation. In our formulation, the D band is excited from a photo-excited electron through a single resonance process in the same way as the G band. It is concluded that, without invoking an artificial assumption, the D band is closely related to the orbital dependence of the electron-phonon matrix element, the special nature of the armchair edge, and optical anisotropy [12].

This paper is organized as follows. In Sec. 2 we observe that a graphene molecular orbital and wave vector are closely correlated. This correlation is both an important factor in terms of understanding the D band and an essential feature of graphene. In Sec. 3 the properties of the D band are deduced from three factors. The importance of the electron-phonon matrix element and the role of the armchair edge in the

excitation mechanism of the D band are explained in detail. In Sec. 4 we show some predictions obtained with our model. Future prospects and our conclusion are given in Sec. 5 and Sec. 6, respectively.

2. Bonding and antibonding orbitals

Graphene's hexagonal unit cell has two carbon atoms, denoted by A and B in Fig. 1, and the electron's wave function ψ is written as a linear combination of $2p_z$ atomic orbitals of the A and B atoms, $\chi_{\rm A}$ and $\chi_{\rm B}$. When we apply Bloch's theorem to graphene, we obtain ψ and the band structure as a function of the wave vector $\mathbf{k}$ [13,14]. In the Brillouin zone (BZ) of graphene, there are two points, namely the K and K$'$ points, where the conduction and valence bands touch each other. The orbitals of the states near the K point take the form of

$$\psi^s_{\rm K}(\mathbf{k}) = \frac{1}{\sqrt{2}}\left(e^{-i\Theta(\mathbf{k})}\chi_{\rm A} + s\chi_{\rm B}\right), \tag{1}$$

where the phase $\Theta \in [0, 2\pi]$ is the polar angle between vector $\mathbf{k}$ measured from the K point and the k_x-axis (see Fig. 1), and $s = \pm 1$ is the band index ($s = +1$ is the π^*-band and $s = -1$ π-band). The orbitals of the states near the K$'$ point are written as

$$\psi^s_{\rm K'}(\mathbf{k}) = \frac{1}{\sqrt{2}}\left(-e^{i\Theta'(\mathbf{k})}\chi_{\rm A} + s\chi_{\rm B}\right), \tag{2}$$

where Θ' is the polar angle defined with respect to the K$'$ point as shown in Fig. 1.

Figure 1. Graphene unit cell and BZ. The K (K$'$) point is located at $\mathbf{k}_{\rm F} = (4\pi/3a, 0)$ $(-\mathbf{k}_{\rm F})$, where a is the lattice constant. The positions of the bonding and antibonding orbitals are marked by red and blue points on the iso-energy sections of the Dirac cones (circles). The Raman D band is composed of zone-boundary A_{1g} modes that consist only of C-C bond stretching motions. The armchair edge identifies a state at (k_x, k_y) with a state at $(-k_x, k_y)$, and causes the BZ holding.

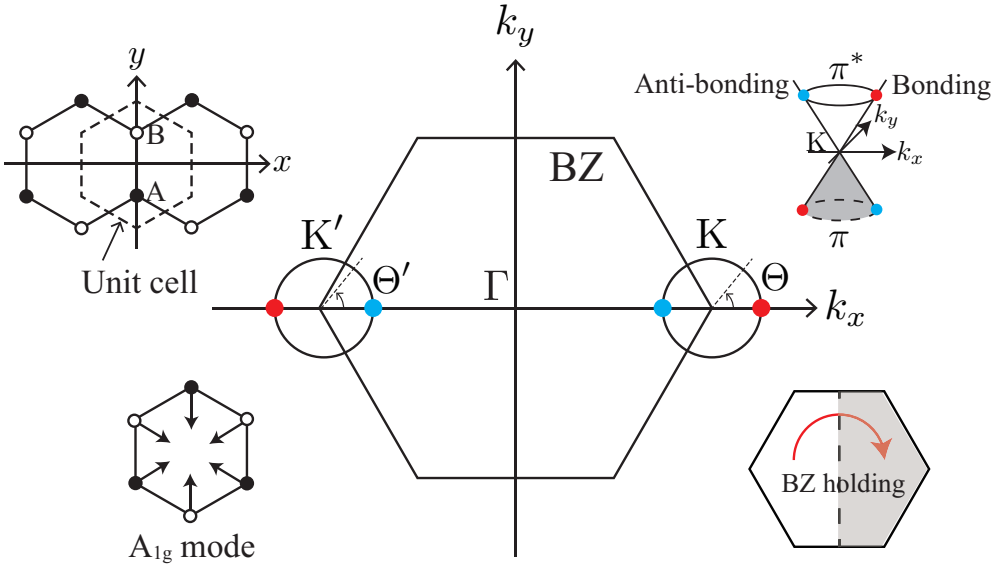

In Eq. (1), the bonding and antibonding orbitals ($\chi_{\rm A}+\chi_{\rm B}$ and $-\chi_{\rm A}+\chi_{\rm B}$) are located at $\Theta=0$ and π, respectively, on the iso-energy section of the π^*-band ($s=+1$). The orbital with a general Θ is a linear combination of the bonding and antibonding orbitals. In Eq. (2), the bonding and antibonding orbitals are located at $\Theta'=\pi$ and 0, respectively, on the iso-energy section of the π^*-band. As we can see in Fig. 1, the bonding (antibonding) orbitals are located symmetrically on the k_x-axis with respect to the Γ point, which is one of the most important characteristics of the BZ of graphene.

The orbitals Eqs. (1) and (2) can be derived from an effective model for graphene, that is, a massless Dirac equation, in the following manner. The energy eigenequation is written as

$$E\psi=\hat{H}\psi=v_{\rm F}\begin{pmatrix}\boldsymbol{\sigma}\cdot\hat{\mathbf{p}} & 0\\ 0 & \boldsymbol{\sigma}'\cdot\hat{\mathbf{p}}\end{pmatrix}\begin{pmatrix}\psi_{\rm K}(\mathbf{r})\\ \psi_{\rm K'}(\mathbf{r})\end{pmatrix}, \tag{3}$$

where $v_{\rm F}$ is the Fermi velocity, $\hat{\mathbf{p}}=(\hat{p}_x,\hat{p}_y)$ is a momentum operator, 0 in the off-diagonal terms represents a 2×2 null matrix, and $\boldsymbol{\sigma}=(\sigma_x,\sigma_y)$ and $\boldsymbol{\sigma}'=(-\sigma_x,\sigma_y)$ are 2×2 Pauli spin matrices:

$$\sigma_x=\begin{pmatrix}0 & 1\\ 1 & 0\end{pmatrix},\quad \sigma_y=\begin{pmatrix}0 & -i\\ i & 0\end{pmatrix}. \tag{4}$$

The massless Dirac equation in Eq. (3) is decomposed into two Weyl's equations for the K and K′ valleys: $E\psi_{\rm K}(\mathbf{r})=v_{\rm F}\boldsymbol{\sigma}\cdot\hat{\mathbf{p}}\psi_{\rm K}(\mathbf{r})$ and $E\psi_{\rm K'}(\mathbf{r})=v_{\rm F}\boldsymbol{\sigma}'\cdot\hat{\mathbf{p}}\psi_{\rm K'}(\mathbf{r})$, respectively. To reproduce Eq. (1), we assume the plane wave solution $\psi_{\rm K}(\mathbf{r})=e^{i\mathbf{k}\cdot\mathbf{r}}\psi_{\rm K}(\mathbf{k})/\sqrt{V}$, and obtain the energy eigenequation $\hbar v_{\rm F}\boldsymbol{\sigma}\cdot\mathbf{k}\psi_{\rm K}(\mathbf{k})=E\psi_{\rm K}(\mathbf{k})$. Then, the corresponding energy eigenvalue and eigenstate are easy to find using $k_x\mp ik_y=|\mathbf{k}|e^{\mp i\Theta(\mathbf{k})}$ as $E=s\hbar v_{\rm F}|\mathbf{k}|$ and

$$\psi^s_{\rm K}(\mathbf{k})=\frac{1}{\sqrt{2}}\begin{pmatrix}e^{-i\Theta(\mathbf{k})}\\ s\end{pmatrix}. \tag{5}$$

This is identical to Eq. (1) by setting

$$\chi_{\rm A}=\begin{pmatrix}1\\ 0\end{pmatrix},\quad \chi_{\rm B}=\begin{pmatrix}0\\ 1\end{pmatrix}. \tag{6}$$

Similarly, we can check that Eq. (2) is the solution of $\hbar v_{\rm F}\boldsymbol{\sigma}'\cdot\mathbf{k}\psi_{\rm K'}(\mathbf{k})=E\psi_{\rm K'}(\mathbf{k})$, which is given by

$$\psi^s_{\rm K'}(\mathbf{k})=\frac{1}{\sqrt{2}}\begin{pmatrix}-e^{i\Theta'(\mathbf{k})}\\ s\end{pmatrix}. \tag{7}$$

The Dirac equation is very helpful as regards understanding the mechanism of a result in terms of symmetry and momentum conservation. In particular, the fact that the Dirac equation is composed of a multiplication of the Pauli matrices (for the A and B atoms) and momentum operators makes it easy to recognize that the orbital (the pattern of the linear combination of $\chi_{\rm A}$ and $\chi_{\rm B}$) is dependent on the wave vector of the particle. In the following, we refer to the Dirac equation for graphene in order to capture the essential features of a result. The graphene Dirac equation differs from the original Dirac equation in the following respect: the wave function ψ in the graphene Dirac equation has 4 components consisting of two orbitals ($\chi_{\rm A}$ and $\chi_{\rm B}$) and two valleys (K and K′), while those in the original Dirac equation are two spin states (up and down spins) and two chiralities (left- and right-handed) [15]. Thus, the orbital degree of freedom is commonly referred to as the pseudo-spin.

3. Light polarization dependence of D band intensity

In this section we show that the light polarization dependence of the D band originates from three factors. The first factor concerns the nature of the electron-phonon interaction for the A_{1g} mode, which will be explained in Sec. 3.1. The second factor is a modification of the BZ by the armchair edge, which will be explored in Sec. 3.2. In Sec. 3.3, we describe the third factor, which concerns the interaction between electrons and a polarized laser light. In Sec. 3.4, we construct the D band polarization formula, by combining the three factors.

3.1. Dominance of intervalley backward scattering

Suppose that an electron has been excited into the π^*-band by a laser light [Fig. 2(a)]. When a photo-excited electron emits an A_{1g} mode, there is a strong probability that the electron will undergo (intervalley) backward scattering, as shown by the real space diagram in Fig. 2(b). In the k-space, the change in the exact (approximate) intervalley backward scattering is denoted by the black (orange and green) solid arrow. Although the forward scattering denoted by the dashed arrow may be allowed by momentum conservation, it never takes place because orbitals suppress the corresponding electron-phonon matrix element. This dominance of intervalley backward scattering originates from the characteristic feature of an A_{1g} mode, namely that the vibration consists only of bond shrinking/stretching motions, as shown by the displacement vectors in Fig. 1. Mathematically, this characteristic of the A_{1g} mode is described by the fact that the electron-phonon interaction, $\hat{H}_{\rm ep}(D)$, satisfies

$$\chi_{\rm A}^\dagger \hat{H}_{\rm ep}(D)\chi_{\rm B} = \chi_{\rm B}^\dagger \hat{H}_{\rm ep}(D)\chi_{\rm A} = g_{\rm ep}, \tag{8}$$

$$\chi_{\rm A}^\dagger \hat{H}_{\rm ep}(D)\chi_{\rm A} = \chi_{\rm B}^\dagger \hat{H}_{\rm ep}(D)\chi_{\rm B} = 0, \tag{9}$$

where $g_{\rm ep}$ is a coupling constant for bond stretching. With these $\hat{H}_{\rm ep}(D)$ conditions, we obtain the electron-phonon matrix element squared $|M|^2 = |\psi^{s'}_{\rm K'}(\Theta')^\dagger \hat{H}_{\rm ep}(D)\psi^{s}_{\rm K}(\Theta)|^2$ using Eqs. (1) and (2) as

$$|M|^2 = \frac{g_{\rm ep}^2}{2}\left\{1 - ss'\cos(\Theta' - \Theta)\right\}. \tag{10}$$

Equation (10) shows that, for intraband scattering ($ss' = 1$), the scattering probability of the exact backward scattering ($\Theta' = \Theta + \pi$) is maximum, while that of the exact forward scattering ($\Theta' = \Theta$) vanishes.

When the energy of a photo-excited electron is much larger than the phonon energy ($\simeq 0.15$ eV), we can assume that no significant energy shift occurs as a result of the inelastic scattering. For the exact backward scattering, the A_{1g} wave vector relates to the photo-excited electron wave vector as $\mathbf{q} = -2\mathbf{k}$, where $\mathbf{q}$ ($\mathbf{k}$) is the wave vector of the A_{1g} mode (photo-excited electron) measured from the K point. This relationship between $\mathbf{k}$ and $\mathbf{q}$ shows that the orbitals effectively relate the electron wave vector $\mathbf{k}$ to the A_{1g} wave vector $\mathbf{q}$. [1]

[1] Thus, the orbital dependence of the electron-phonon matrix element justifies the basic idea of the quasi-selection rule for the D band proposed by several authors [16,17]. As examined in Sec. 4.1, the relationship between $\mathbf{k}$ and $\mathbf{q}$ ($\mathbf{q} = -2\mathbf{k}$) is important when we discuss the dispersive behavior of the D band. $2\hbar v_{\rm F}|\mathbf{k}|$ is approximately equal to the laser excitation energy E_L and $\hbar v_{\rm F}|\mathbf{q}|$ changes linearly with changing E_L.

Figure 2. Mechanism of D band intensity enhancement at armchair edge. (a) A photo-excited electron near the K point. (b) The electron-phonon interaction of an zone-boundary A_{1g} mode results in the dominance of intervalley backward scattering. (c) The BZ holding leads to the appearance of two special electronic states (with the bonding [red] and antibonding [blue] orbitals): an A_{1g} mode can be excited from them through a first-order Raman process. In real space, this is represented by the fact that the color of the points does not change while emitting an A_{1g} mode.

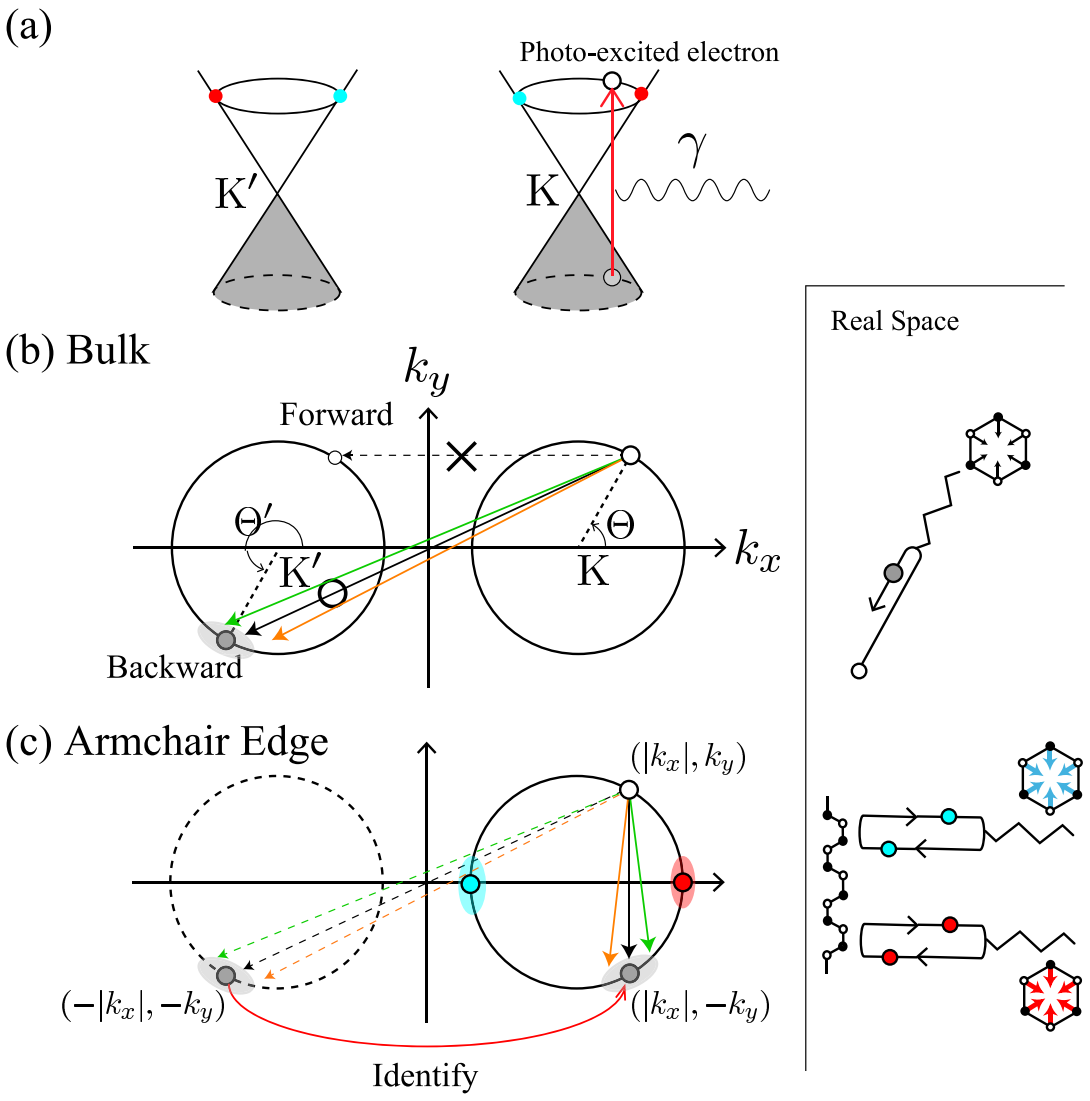

It is straightforward to reproduce Eq. (10) in the framework of the graphene Dirac equation. The electron-phonon interaction for an A_{1g} mode with wave vector $\mathbf{q}$ is written as [18]

$$\hat{H}_{\rm ep}(D_{\mathbf{q}}) = g_{\rm ep} \begin{pmatrix} 0 & e^{-i\mathbf{q}\cdot\mathbf{r}}\sigma_x \\ e^{i\mathbf{q}\cdot\mathbf{r}}\sigma_x & 0 \end{pmatrix}, \tag{11}$$

and the matrix element M is given by

$$\begin{aligned} M &= \int_V d^2\mathbf{r}\psi^{s'}_{\rm K'}(\mathbf{r})^\dagger \hat{H}_{\rm ep}(D_{\mathbf{q}})\psi^{s}_{\rm K}(\mathbf{r}) \\ &= \left(\frac{1}{V}\int_V d^2\mathbf{r}e^{i(\mathbf{k}+\mathbf{q}-\mathbf{k}')\cdot\mathbf{r}}\right)\left(\psi^{s'}_{\rm K'}(\mathbf{k}')^\dagger\sigma_x\psi^{s}_{\rm K}(\mathbf{k})\right). \end{aligned} \tag{12}$$

The last line is written as a multiplication of two parts: the first part represents momentum conservation and the wave vector of the scattered electron $\mathbf{k}'$ is given by $\mathbf{k}' = \mathbf{k} + \mathbf{q}$. The second part gives Eq. (10). In addition to momentum conservation, we can use energy conservation to obtain $v_{\rm F}|\mathbf{k}'| = v_{\rm F}|\mathbf{k}| - \omega_{\mathbf{q}}$, where $\omega_{\mathbf{q}}$ is the frequency of A_{1g}. Thus, when $\hbar v_{\rm F}|\mathbf{k}| \gg \hbar\omega_{\mathbf{q}}$, we have $|\mathbf{k}'| \simeq |\mathbf{k}|$. Since the orbital part results in the dominance of intervalley backward scattering, we obtain $\mathbf{k}' \simeq -\mathbf{k}$. As a result, $\mathbf{q} \simeq -2\mathbf{k}$ is satisfied.

3.2. Brillouin zone holding

The dominance of intervalley backward scattering causes an enhancement of the D band Raman intensity if Brillouin zone holding (BZH) by the armchair edge is taken into account [12]. Here, BZH means that, in the BZ of graphene shown in Fig. 1, a state with (k_x, k_y) is identical to a state with $(-k_x, k_y)$ and that the correct BZ is given by the positive k_x region of the original BZ of graphene [19]. In Fig. 2(c), as a consequence of BZH, the final state in the intervalley backward scattering event is identified with the state near the K point. Namely, the state with $(-|k_x|, -k_y)$ near the K′ point is identified with the state with $(|k_x|, -k_y)$ near the K point. So, in the held BZ, the change in a photo-excited electron is $(|k_x|, k_y) \rightarrow (|k_x|, -k_y)$, as shown by the solid arrow in Fig. 2(c). Generally, the probability of a process in the held BZ is given by replacing Θ' with $\pi - \Theta'$ in Eq. (10) as

$$|M_{\rm BZH}|^2 = \frac{g_{\rm ep}^2}{2}\left\{1 + ss'\cos(\Theta' + \Theta)\right\}, \tag{13}$$

and this transition probability is indeed maximum when $\Theta' = -\Theta$. When $\Theta' = \Theta$ and $s' = s$ in Eq. (13), the final state coincides with the initial state, which is the condition of a first-order Raman process. In this case, the probability is given by

$$|M_{\rm BZH}|^2 = g_{\rm ep}^2\cos^2\Theta, \tag{14}$$

which takes its maximum value for $\Theta = 0$ and π. This shows that the states near the k_x-axis (or the states with bonding and antibonding orbitals) can contribute to the D band intensity through a first-order Raman process.

BZH originates from the fact that a special standing wave is formed by an armchair edge. The standing wave is constructed by the antisymmetric combination of an incident plane wave with $\mathbf{k} = (k_x, k_y)$ and

a scattered plane wave with $\mathbf{k}' = (-k_x, k_y)$ as $e^{ik_y y}(e^{ik_x x} - e^{-ik_x x}) \propto e^{ik_y y}\sin(k_x x)$. A symmetric combination does not satisfy the boundary condition for the armchair edge. Note that $\sin(k_x x)$ does not change when k_x is replaced with $-k_x$, except for the unimportant change in the overall sign. More importantly, the orbital part Eq. (1) does not change when there is the reflection at the armchair edge, as we can confirm by replacing Θ' with $\pi - \Theta$ in Eq. (2) [20]. The same orbitals are superposed to form a standing wave at the armchair edge. Thus, the total wave function becomes

$$\psi^s_{\rm a}(\mathbf{k}) = N\left\{e^{i\mathbf{k}\cdot\mathbf{r}}\begin{pmatrix}e^{-i\Theta(\mathbf{k})}\\ s\end{pmatrix} - e^{i\mathbf{k}'\cdot\mathbf{r}}\begin{pmatrix}-e^{i\Theta'(\mathbf{k}')}\\ s\end{pmatrix}\right\} = N' e^{ik_y y}\sin(k_x x)\begin{pmatrix}e^{-i\Theta(\mathbf{k})}\\ s\end{pmatrix}, \qquad (15)$$

where N (N') is a normalization constant [19]. The standing wave does not change with the replacement $k_x \to -k_x$, and therefore the correct BZ of the standing wave is given solely by the positive k_x region to avoid double counting. It is noteworthy that BZH is specific to the armchair edge and is not applicable to a zigzag edge. The absence of BZH at a zigzag edge is due to the orbital part changes with the reflection of an electron at the zigzag edge and the different orbitals are superposed to form a standing wave. The standing wave for a zigzag edge is written as

$$\psi^s_{\rm z}(\mathbf{k}) = N e^{ik_x x}\left\{e^{ik_y y}\begin{pmatrix}e^{-i\Theta(\mathbf{k})}\\ s\end{pmatrix} - e^{-ik_y y}\begin{pmatrix}e^{i\Theta(\mathbf{k})}\\ s\end{pmatrix}\right\} = N' 2i e^{ik_x x}\begin{pmatrix}\sin(k_y y - \Theta))\\ s\sin(k_y y)\end{pmatrix}, \qquad (16)$$

which is not invariant with the replacement $k_y \to -k_y$ unless $\Theta = 0$ or π. Thus, it needs a second-order process to activate a phonon mode with nonzero $\mathbf{q}$ (see Fig. 3) and a first-order Raman band (except the G band) cannot appear at the zigzag edge. Although the intensity is not comparable to that of G or D bands, we can expect a second-order band to appear at the zigzag edge. The D' band [21,22] (not the D band) may be such a second-order Raman band that can be described by the double resonance model.

Figure 3. A process that causes the D' band at the zigzag edge. Phonon excitation ($\mathbf{q} \neq 0$) accompanied by a change in the electronic states, which shows that the phonon does not appear through a first-order process. Note that, in the right diagram, the color of the points changes after the phonon is emitted.

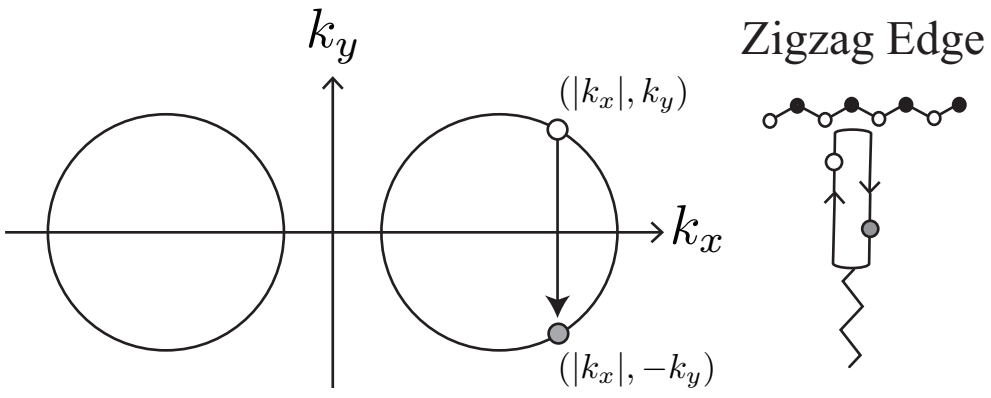

The standing wave at the armchair edge can be expressed in the framework of the Dirac equation as

$$\psi^{s}_{\mathrm{a},\mathbf{k}}(\mathbf{r}) = Ne^{ik_y y}\begin{pmatrix} e^{+ik_x x}e^{-i\Theta(\mathbf{k})} \\ e^{+ik_x x}s \\ e^{-ik_x x}e^{-i\Theta(\mathbf{k})} \\ e^{-ik_x x}s \end{pmatrix} = Ne^{ik_y y}\begin{pmatrix} e^{+ik_x x} \\ e^{-ik_x x} \end{pmatrix} \otimes \frac{1}{\sqrt{2}}\begin{pmatrix} e^{-i\Theta(\mathbf{k})} \\ s \end{pmatrix}, \tag{17}$$

where $\mathbf{k}$ denotes the wave vector measured from the Dirac point in the held BZ and $\otimes$ represents the direct product of the valley and the orbital. It can be confirmed that Eq. (17) reproduces Eq. (13), by calculating the expectation value of $\hat{H}_{\mathrm{ep}}(D_{\mathbf{q}})$ of Eq. (11) with respect to Eq. (17),

$$\begin{aligned} M_{\mathrm{BZH}} &= \int_V d^2\mathbf{r}\psi^{s'}_{\mathrm{a},\mathbf{k}'}(\mathbf{r})^\dagger \hat{H}_{\mathrm{ep}}(D_{\mathbf{q}})\psi^{s}_{\mathrm{a},\mathbf{k}}(\mathbf{r}) \\ &= \delta(q_x - k_x - k'_x)\frac{1}{2}\left\{\delta(k_y + q_y - k'_y) + \delta(k_y - q_y - k'_y)\right\}\frac{g_{\mathrm{ep}}}{2}\left(e^{i\Theta'}s + s'e^{-i\Theta}\right), \end{aligned} \tag{18}$$

where we used $N^2\int dy e^{i(k_y \pm q_y - k'_y)y}\int dx e^{\pm i(q_x - k_x - k'_x)x} = (1/2)\delta(k_y \pm q_y - k'_y)\delta(q_x - k_x - k'_x)$. For $\mathbf{k}' = \mathbf{k}$ (i.e., for a first order Raman process), Eq. (14) is reproduced, and momentum conservation gives $\mathbf{q} = (2k_x, 0)$.

3.3. Optical anisotropy

The third factor is the polarization dependence of optical transitions. To supply photo-excited electrons to the states with bonding and antibonding orbitals on the k_x-axis, the polarization of incident laser light must be set parallel to the armchair edge (y-axis), as shown in Fig. 4(b). The photo-excited electrons on the k_x-axis emit A_{1g} modes without changing their positions [see Fig. 4(a)]. Meanwhile, when the polarization of the incident laser light is set perpendicular to the armchair edge, the x-polarized light supplies the states on the k_y-axis with photo-excited electrons [see Fig. 4(c)]. The electrons near the k_y-axis change their positions in the held BZ when they emit A_{1g} modes [see Fig. 2(b)], and these electrons on the k_y-axis do not contribute to the D band intensity. As a result, the D band can be strongly dependent on the laser light polarization: the D band intensity is enhanced (suppressed) when the polarization of the incident laser light is parallel (perpendicular) to the armchair edge.

The optical anisotropy is due to the Θ dependence of the optical matrix element [23]. Namely, for y (x) polarized light, $\vec{E}_y$ ($\vec{E}_x$), the optical matrix element squared is proportional to $\cos^2\Theta$ ($\sin^2\Theta$) as

$$|M_{\mathrm{opt}}|^2 = \begin{cases} g^2_{\mathrm{e}\gamma}\cos^2\Theta & \text{for } \vec{E}_y, \\ g^2_{\mathrm{e}\gamma}\sin^2\Theta & \text{for } \vec{E}_x, \end{cases} \tag{19}$$

where $g_{\mathrm{e}\gamma}$ denotes an electron-light coupling constant. The electrons near the k_x (k_y)-axis are dominantly photo-excited by $\vec{E}_y$ ($\vec{E}_x$) [see Fig. 4(b) and (c)]. For the general polarization direction of incident laser light $\mathbf{E}$, M_{opt} is proportional to the direct product of $\mathbf{E}$ and $\hat{\mathbf{k}}$ ($\equiv \mathbf{k}/|\mathbf{k}|$) as $M_{\mathrm{opt}} \propto \mathbf{E} \times \hat{\mathbf{k}}$.

Although Eq. (19) was derived without taking account of the edge, it turns out that a similar optical matrix element is obtained for the standing waves [24]. Here, let us use the Dirac equation of Eq. (3) to

Figure 4. Light polarization dependence of the D band. (a) An A_{1g} phonon is excited through a first-order process from the electrons with bonding and antibonding orbitals on the k_x-axis. (b) To supply a photo-excited electron to the states on the k_x axis, the laser light polarization must be parallel to the y-axis or the armchair edge. (c) $\vec{E}_x$ can produce a photo-excited electron at the k_y-axis. Such an electron changes its position when it emits an A_{1g} mode, and thus it cannot contribute to the D band.

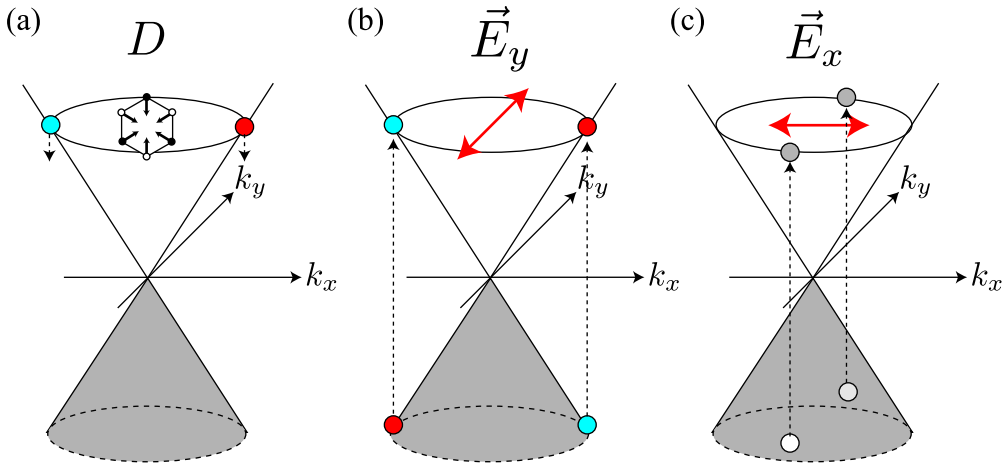

obtain the matrix element that includes the effect of the armchair edge. The electron-light interaction is given by replacing $\hat{\mathbf{p}}$ with $\hat{\mathbf{p}} - e\mathbf{A}$ in Eq. (3) as

$$\hat{H} = v_{\rm F} \begin{pmatrix} \boldsymbol{\sigma} \cdot (\hat{\mathbf{p}} - e\mathbf{A}) & 0 \\ 0 & \boldsymbol{\sigma}' \cdot (\hat{\mathbf{p}} - e\mathbf{A}) \end{pmatrix}, \tag{20}$$

where $\mathbf{A}$ is the vector potential of light. Since the Maxwell equation gives $\mathbf{E} = -\partial\mathbf{A}/\partial t$, the vector directions of $\mathbf{E}$ and $\mathbf{A}$ are the same. The optical matrix element is defined using Eq. (17) as

$$M_{\rm opt} = -ev_{\rm F} \int d^2\mathbf{r} \psi^{+1}_{{\rm a},\mathbf{k}'}(\mathbf{r})^\dagger \begin{pmatrix} \boldsymbol{\sigma} \cdot \mathbf{A} & 0 \\ 0 & \boldsymbol{\sigma}' \cdot \mathbf{A} \end{pmatrix} \psi^{-1}_{{\rm a},\mathbf{k}}(\mathbf{r}). \tag{21}$$

For the y-polarized light $\mathbf{A} = (0, A_y)$, $M_{\rm opt}$ is nonzero only for a direct transition ($\mathbf{k}' = \mathbf{k}$) and the orbital gives $\cos\Theta$. For the x-polarized light $\mathbf{A} = (A_x, 0)$, $M_{\rm opt}$ includes the integral $(1/L)\int_0^L dx \sin(k_x - k'_x)x$ and the orbital gives $(-e^{i\Theta'} + e^{-i\Theta})/2$. Since the integral vanishes when $k_x = k'_x$, a direct transition does not take place. The possible transitions are indirect transitions $k_x \neq k'_x$. For $k_x - k'_x = n\pi/L$ (n is an odd number), we obtain $2/(n\pi)$ by performing the integral. The momentum change in an indirect transition is inversely proportional to the distance (L) from the armchair edge where the standing wave is a good approximation. Since the change in the wave vector is negligible when L is large, we may assume $\Theta' \simeq \Theta$. Then the orbital leads to $-i\sin\Theta$, which reproduces Eq. (19). This feature of the indirect transition for the x-polarized light has been examined with a more mathematically rigorous method using a lattice tight-binding model [24].

3.4. D band polarization formula

We combine Eqs. (14) and (19) to derive the polarization formula of the D band. The probability of a first-order Raman process that an electron with Θ in the π-band is excited into the π^*-band by $\vec{E}_i$

($i = \{x, y\}$), and then the photo-excited electron emits the A_{1g} mode, and finally the electron with Θ emits a light with $\vec{E}_j$ is given by

$$|M_{ji}(\Theta)|^2 = |M_{\rm opt}(\vec{E}_j)|^2 |M_{\rm BZH}(\Theta)|^2 |M_{\rm opt}(\vec{E}_i)|^2 = g_{\rm e\gamma}^4 g_{\rm ep}^2 \begin{cases} \cos^6\Theta & (ji) = (yy) \\ \cos^4\Theta \sin^2\Theta & (xy) \text{ or } (yx) \\ \cos^2\Theta \sin^4\Theta & (xx). \end{cases} \quad (22)$$

Note that the wave vector of the A_{1g} mode is completely fixed by Θ and $|\mathbf{k}|$ (or E_L) as $q_x = -2|\mathbf{k}|\cos\Theta$. Phonons with different momenta are distinguishable in principle. We have different final states for different Θ values, and to calculate the D band intensity, we need to sum over all possible final states by operating $|M_{ji}(\Theta)|^2$ with $\int_0^{2\pi} d\Theta$. Because $\int_0^{2\pi} \cos^2\Theta \sin^4\Theta d\Theta / \int_0^{2\pi} \cos^6\Theta d\Theta = 1/5$, the polarization dependence of the D band intensity is written as

$$I_D(\theta_{\rm out}, \theta_{\rm in}) \propto \begin{pmatrix} \cos^2\theta_{\rm out} & \sin^2\theta_{\rm out} \end{pmatrix} \begin{pmatrix} 1 & 1/5 \\ 1/5 & 1/5 \end{pmatrix} \begin{pmatrix} \cos^2\theta_{\rm in} \\ \sin^2\theta_{\rm in} \end{pmatrix}, \quad (23)$$

where $\theta_{\rm in}$ ($\theta_{\rm out}$) denotes the angle of an incident (scattered) electric field with respect to the armchair edge. [2] When the VV configuration ($\theta_{\rm out} = \theta_{\rm in}$) is used, the polarization dependence is approximated by $I_D^{VV}(\theta_{\rm in}) \simeq I\cos^4\theta_{\rm in}$. On the other hand, when the VH configuration ($\theta_{\rm out} = \theta_{\rm in} + \pi/2$) is used, the polarization dependence is approximated by $I_D^{VH}(\theta_{\rm in}) \simeq I\cos^2\theta_{\rm in}\sin^2\theta_{\rm in}$. These results are consistent with the experiment reported by Cançado et al [7]. Without a polarizer for the scattered light, we have

$$I_D(\theta_{\rm in}) \propto \left(\int_0^{2\pi} d\Theta \cos^4\Theta\right) \cos^2(\theta_{\rm in}) + \left(\int_0^{2\pi} d\Theta \cos^2\Theta \sin^2\Theta\right) \sin^2(\theta_{\rm in}). \quad (24)$$

Because $\int_0^{2\pi} \cos^2\Theta\sin^2\Theta d\Theta / \int_0^{2\pi} \cos^4\Theta d\Theta = 1/3$, it may be rewritten as $I_D(\theta_{\rm in}) \propto \cos^2(\theta_{\rm in}) + (1/3)\sin^2(\theta_{\rm in})$. With (Without) a polarizer for scattered light, the depolarization ratio $I_D(90^\circ)/I_D(0^\circ)$ is $1/5$ ($1/3$). Generally, the D band polarization dependence is fitted using an empirical formula

$$I_D(\theta_{\rm in}) \propto \cos^2(\theta_{\rm in}) + b\sin^2(\theta_{\rm in}) + c, \quad (25)$$

where c is a constant, which probably originates from a defect beside the edge. The constants b and c determine the depolarization ratio: $I_D(90^\circ)/I_D(0^\circ) = (b + c)/(1 + c)$. When c is much larger than unity, the polarization behavior is obscured. If c is negligible, a smaller depolarization ratio ($b = 1/5$) is expected when a polarizer is used for the scattered light.

4. Predictions of our model

We have seen that the D band has a direct relationship to the bonding and antibonding orbitals (that is, an A_{1g} mode is excited through the first-order Raman process only from these orbitals). This conclusion has been derived based on two factors: the dominance of intervalley backward scattering (Sec. 3.1), and

[2] In calculating the D band Raman intensity, it is incorrect to sum over intermediate states specified by the electron's wave vector $\mathbf{k}$, such as $|\sum_{\mathbf{k}} M_{ji}(\Theta(\mathbf{k}))|^2$. Because the phonon wave vector relates to the electron wave vector through $\mathbf{q} = -2\mathbf{k}$, $\sum_{\mathbf{k}}$ actually means a summation for different phonons (final states). Thus, the Raman intensity is proportional to $\sum_{\mathbf{q}} |M_{ji}(\Theta(\mathbf{q}))|^2$ or $\int_0^{2\pi} d\Theta |M_{ji}(\Theta)|^2$.

Figure 5. Polar plot for the D band intensity. The parameters for the solid curve are $a = 1$, $b = 1/3$, and $c = 0$, while those for the dashed curve are $a = 1$ and $b = c = 0$.

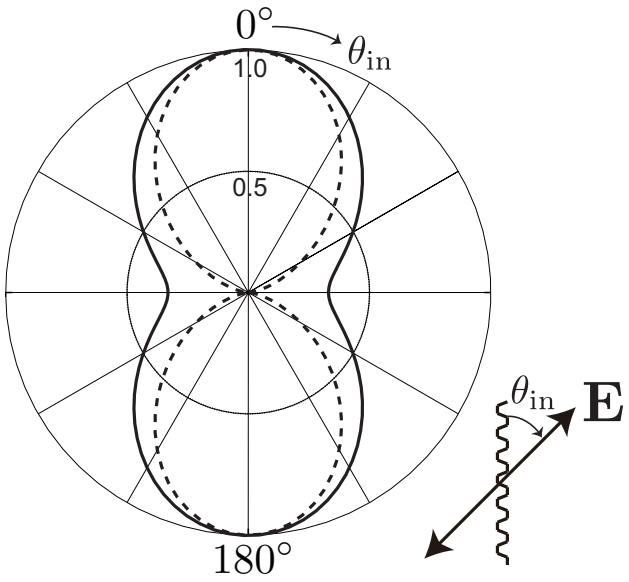

BZH by the armchair edge (Sec. 3.2). In this section, we report some consequences that are derived from these factors.

4.1. The origin of Dispersive Behavior

The D band frequency ω_D increases linearly with increasing excitation energy E_L as $\partial\omega_D/\partial E_L \sim 50$ cm^{-1}/eV, which is known as dispersive behavior [9,25–27]. In a previous paper [28], we pointed out that the dispersive behavior is mainly attributed to a quantum mechanical correction (self-energy) to the A_{1g} frequency. The modified energy of the A_{1g} mode is written as $\hbar\omega + \mathrm{Re}\Pi_\mu(q,\omega)$, where ω is the bare frequency and $\Pi_\mu(q,\omega)$ represents the self-energies of the A_{1g} modes induced by electron-phonon interaction. The self-energy of an A_{1g} mode with $q = |\mathbf{q}|$ is defined as

$$\Pi_\mu(q,\omega) \equiv \sum_{s,s'}\sum_{\mathbf{k}} \frac{(f^s_{\mathbf{k},\mu} - f^{s'}_{\mathbf{k}+\mathbf{q},\mu})g_s|M|^2}{\hbar\omega + s\hbar v_{\rm F}k - s'\hbar v_{\rm F}|\mathbf{k}+\mathbf{q}| + i\epsilon}, \tag{26}$$

where ϵ is a positive infinitesimal, $f^s_{\mathbf{k},\mu} = \lim_{\beta\to\infty}(1 + e^{\beta(sv|\mathbf{k}|-\mu)})^{-1}$ is the Fermi distribution function with finite doping μ, and $g_s = 2$ represents spin degeneracy. The electron-phonon matrix element squared $|M|^2$ is constructed in Eq. (10) as $|M|^2 = \frac{g^2_{\rm ep}}{2}\{1 - ss'\cos(\Theta'(\mathbf{k}+\mathbf{q}) - \Theta(\mathbf{k}))\}$.

In the continuum limit of $\mathbf{k}$, $\Pi_\mu(q,\omega)$ is calculated analytically. The expression of the real part is given by

$$\begin{aligned}
&\mathrm{Re}\Pi_\mu(q,\omega)/G_{\rm ep} = 4\pi\mu \\
&+ \hbar\pi\sqrt{\omega^2 - v^2_{\rm F}q^2}\theta_{\omega - v_{\rm F}q}\left[-g\left(\frac{\hbar\omega+2\mu}{\hbar v_{\rm F}q}\right) + \theta_{\frac{\hbar\omega-\hbar v_{\rm F}q}{2}-\mu}\, g\left(\frac{\hbar\omega-2\mu}{\hbar v_{\rm F}q}\right) + \theta_{\mu-\frac{\hbar\omega+\hbar v_{\rm F}q}{2}}\, g\left(\frac{2\mu-\hbar\omega}{\hbar v_{\rm F}q}\right)\right] \\
&+ \hbar\pi\sqrt{v^2_{\rm F}q^2 - \omega^2}\theta_{\hbar v_{\rm F}q-\hbar\omega}\left\{\theta_{\frac{\hbar v_{\rm F}q-\hbar\omega}{2}-\mu}\left[\frac{\pi}{2} - \sin^{-1}\left(\frac{\hbar\omega+2\mu}{\hbar v_{\rm F}q}\right)\right] + \theta_{\frac{\hbar v_{\rm F}q+\hbar\omega}{2}-\mu}\left[\frac{\pi}{2} - \sin^{-1}\left(\frac{2\mu-\hbar\omega}{\hbar v_{\rm F}q}\right)\right]\right\},
\end{aligned} \tag{27}$$

Figure 6. A 3d plot of $\mathrm{Re}\Pi_\mu(q,\omega_D)$. The variables $\hbar v_\mathrm{F} q$ and μ are given in eV. Note that $\mathrm{Re}\Pi_\mu(q,\omega)$ does not include the q dependence of the bare frequency.

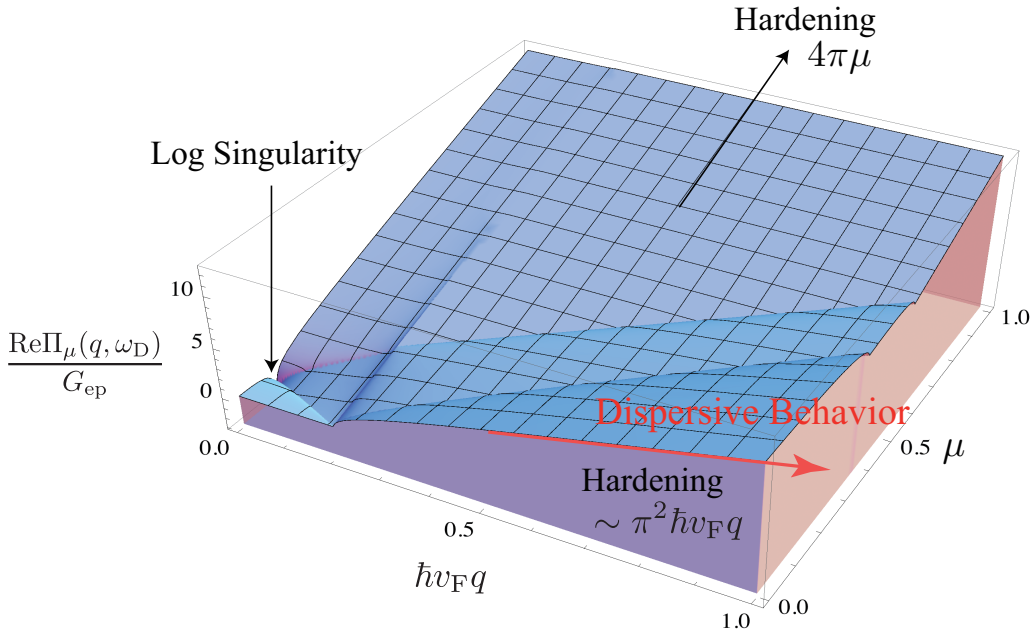

where θ_x denotes a step function satisfying $\theta_{x\geq 0}=1$ and $\theta_{x<0}=0$, $g(x)\equiv \ln(x+\sqrt{x^2-1})$, and $G_\mathrm{ep}\equiv g_\mathrm{ep}^2 V/(2\pi\hbar v_\mathrm{F})^2$ is a (dimensionless) coupling constant. A 3d plot of $\mathrm{Re}\Pi_\mu(q,\omega_D)/G_\mathrm{ep}$ is shown in Fig. 6. Interestingly, $\mathrm{Re}\Pi_\mu(q,\omega_D)$ increases as we increase q. In fact, near the Dirac point, $\mathrm{Re}\Pi_\mu(q,\omega_D)$ follows

$$\mathrm{Re}\Pi_{\mu\sim 0}(q,\omega)\simeq G_\mathrm{ep}\pi^2\hbar v_\mathrm{F} q. \tag{28}$$

Since $\hbar v_\mathrm{F} q\simeq E_L$, the self-energy contributes to the dispersive behavior of the D (or $2D$) band [9,25–27,29]. If we use $G_\mathrm{ep}=5$ cm^{-1}, which is obtained from the broadening data published by Chen et al. [3], the self-energy can account for ~60% of the dispersion because $\mathrm{Re}\Pi_{\mu\simeq 0}(q,\omega_q)\simeq G_\mathrm{ep}\pi^2 E_L$ and $G_\mathrm{ep}\pi^2\simeq 30$ cm^{-1}. It should be emphasized that the self-energy is calculated using only Eq. (10), and any artificial assumption, such as an adiabatic approximation, is not employed when calculating the self-energy. The physical origin of the dispersive behavior is easy to be understood with shifted Dirac cones [28]. In perturbation theory, the mechanism of dispersive behavior is almost the same as the mechanism where the G band exhibits hardening with increasing $|\mu|$.

The dispersive behavior is not an inherent property of the D band but rather is a property of the A_{1g} mode. The armchair edge is involved in the activation of the D band. However, the dispersive behavior itself has nothing to do with the edge. In other words, there are processes that can exhibit dispersive behavior, besides the Raman D band. A good example is the $2D$ band, for which dispersive behavior is observed because the $2D$ band consists of two A_{1g} modes.

4.2. Intravalley Phonons

In addition to the zone-boundary A_{1g} mode, we can determine the effect of BZH on zone-center (intravalley) optical phonon modes: BZH forbids an intravalley transverse optical (TO) mode to appear

as a prominent Raman band at the armchair edge. The Dirac equation is the most useful way of showing this. The electron-phonon interactions for the LO and TO modes with (nonzero) momentum (q_x, q_y) are written as

$$\hat{H}_{\rm LO}(\mathbf{q}) = g_{\rm ep}\frac{e^{i\mathbf{q}\cdot\mathbf{r}}}{|\mathbf{q}|}\begin{pmatrix}\sigma_x q_y - \sigma_y q_x & 0\\ 0 & \sigma_x q_y + \sigma_y q_x\end{pmatrix}, \tag{29}$$

$$\hat{H}_{\rm TO}(\mathbf{q}) = g_{\rm ep}\frac{e^{i\mathbf{q}\cdot\mathbf{r}}}{|\mathbf{q}|}\begin{pmatrix}\sigma_x q_x + \sigma_y q_y & 0\\ 0 & \sigma_x q_x - \sigma_y q_y\end{pmatrix}, \tag{30}$$

and their matrix elements are obtained from Eq. (17) as

$$\begin{aligned} M_{\rm LO}(\mathbf{q}) = {} & \frac{g_{\rm ep}}{|\mathbf{q}|}\delta(-k'_y + q_y + k_y)\times \\ & \{\delta(-k'_x + q_x + k_x)\left[\langle\sigma_x\rangle q_y - \langle\sigma_y\rangle q_x\right] + \delta(-k'_x - q_x + k_x)\left[\langle\sigma_x\rangle q_y + \langle\sigma_y\rangle q_x\right]\}, \end{aligned} \tag{31}$$

$$\begin{aligned} M_{\rm TO}(\mathbf{q}) = {} & \frac{g_{\rm ep}}{|\mathbf{q}|}\delta(-k'_y + q_y + k_y)\times \\ & \{\delta(-k'_x + q_x + k_x)\left[\langle\sigma_x\rangle q_x + \langle\sigma_y\rangle q_y\right] + \delta(-k'_x - q_x + k_x)\left[\langle\sigma_x\rangle q_x - \langle\sigma_y\rangle q_y\right]\}, \end{aligned} \tag{32}$$

where $\langle\sigma_x\rangle \equiv (se^{i\Theta'} + s'e^{-\Theta})/2$ and $\langle\sigma_y\rangle \equiv -i(se^{i\Theta'} - s'e^{-\Theta})/2$. For the TO mode, $M_{\rm TO}(\mathbf{q})$ vanishes in the $q_x \to 0$ limit, due to the interference between the valleys. In the $q_y \to 0$ limit, $\Theta' = \pi - \Theta$ holds, and the orbital of the matrix element, $\langle\sigma_x\rangle$, vanishes when $s' = s$. Thus, the electron-phonon matrix element for the Γ point TO mode is suppressed compared with that of the LO mode: the Γ point TO mode is missing in the G band at the armchair edge [10,20,30,31].

4.3. D Band Splitting

The D band is composed of the (two) A_{1g} modes that are emitted from two electronic states with bonding or antibonding orbitals ($\Theta = 0$ or π). This fact results in the splitting of the D band if the trigonal warping effect is taken into account [12]. The splitting width increases with increasing incident laser energy E_L as

$$\Delta\omega_D = 25\left(\frac{E_L}{\gamma}\right)^2\ [\mathrm{cm}^{-1}], \tag{33}$$

where γ ($\simeq 3$ eV) is the hopping integral between nearest neighbor atoms. This formula is derived by noting that the wave vectors for the two A_{1g} modes that originate from the bonding and antibonding orbitals, are different due to the trigonal warping effect. The difference is estimated with the lattice tight-binding model as [12]

$$\Delta q = \frac{\sqrt{3}}{a}\left(\frac{E_L}{3\gamma}\right)^2. \tag{34}$$

For simplicity, let us assume that the phonon dispersion relation for the D band is isotropic about the Dirac point. From Fig. 7 it is clear that the two phonon modes with q_0 and q_π have different phonon energies, which results in the double peak structure of the D band. The difference between the energy of the phonon mode with q_0 and that with q_π is approximated by

$$\Delta\omega_D = \frac{\partial\omega_D}{\partial q}\Delta q, \tag{35}$$

where $\partial\omega_D/\partial q$ is the slope of the phonon energy dispersion. We interpret the dispersive behavior that occurs as a result of the dispersion relation of the phonon mode. Then we have

$$\frac{\partial\omega_D}{\partial q} = \frac{\partial E_L}{\partial q}\frac{\partial\omega_D}{\partial E_L}. \tag{36}$$

Putting $|\partial E_L/\partial q| = \hbar v_{\rm F}$ in Eq. (36), and combining it with Eqs. (34) and Eq. (35), we obtain Eq. (33).

Figure 7. Two principal wave vectors of the phonons (q_0 and q_π) contributing to the D band. The phonon dispersion relation near the Dirac point. The energy difference between $\omega_D(q_0)$ and $\omega_D(q_\pi)$ appears as two peaks in the D band.

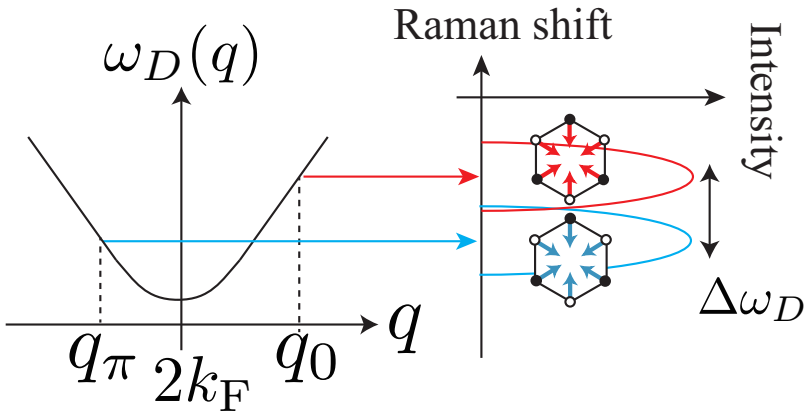

5. Prospects

The D band has a close relationship with the energy gap. A direct relationship between the zone-boundary A_{1g} mode and the energy gap is seen in the Pierls instability at armchair nanoribbons [32,33]. In the Dirac equation, an energy gap is represented by a Dirac mass term that appears in the off-diagonal terms as

$$\hat{H} = \begin{pmatrix} v_{\rm F}\boldsymbol{\sigma}\cdot\hat{\mathbf{p}} & m\sigma_x \\ m^*\sigma_x & v_{\rm F}\boldsymbol{\sigma}'\cdot\hat{\mathbf{p}} \end{pmatrix}. \tag{37}$$

The spectrum has an energy gap $2|m|$, because the energy dispersion is given by $\pm\sqrt{(\hbar v_{\rm F}k)^2+|m|^2}$. The zone-boundary A_{1g} mode is related to the Dirac mass because the electron-phonon interaction [Eq. (11)] appears as a mass term in the Dirac equation: $m \to g_{\rm ep}e^{-i\mathbf{q}\cdot\mathbf{r}}$. The dominance of intervalley backward scattering becomes clear with respect to the mass term, because a nonzero mass tends to stop a massless particle by backward scattering.

Interestingly, the armchair edge itself can be modeled as a singular mass term in the Dirac equation, whereby Eq. (17) is obtained as a solution of the model [34]. This theoretical framework leads us to find a relationship between the dominance of intervalley backward scattering represented by Eq. (10) and BZH. To see a connection between them, it is important to recognize that in deriving Eq. (10), the orbital structures of Eqs. (1) and (2) play a decisive role. These orbitals have to relate to each other by mirror symmetry with respect to the x-axis [$x \to -x$ or $k_x \to -k_x$] in Fig. 1. In fact, Eq. (2) is constructed by replacing Θ with $\pi - \Theta'$ in Eq. (1). The orbital should be invariant under this replacement.

Defects, such as a lattice vacancy and a topological defect, are considered to be sources that increase the D band intensity [c-term in Eq. (25)]. This speculation is reasonable, because creating a lattice vacancy inevitably involves the antibonding orbital. Unfortunately, the wave functions and the corresponding BZ in the presence of defects are difficult to construct rigidly in the framework of a tight-binding lattice model. This difficulty prevents us from calculating the electron-phonon matrix element exactly. However, there is the possibility of obtaining a good approximation of the matrix element using the Dirac equation.

6. Conclusion

An orbital and wave vector are the basic idea for a molecular and a crystal, respectively. Knowing the correlation between them is the key to understand the D band. The D band originates from two orbitals: the bonding and antibonding orbitals on the k_x-axis. Observing the D band is the same thing as selecting the two orbitals from the various orbitals that compose the iso-energy section of the Dirac cone. This idea leads us to expect the optical control of edge chiralities [35]. A slight asymmetry between the bonding and antibonding orbitals, induced by the trigonal warping effect, may be important in terms of understanding the stability of the armchair edge under laser light irradiation. A closer study of the D band based on the Dirac equation will be fruitful for a further investigation of the physics of the D band.

Acknowledgments

References

1. Novoselov, K.S.; Geim, A.K.; Morozov, S.V.; Jiang, D.; Katsnelson, M.I.; Grigorieva, I.V.; Dubonos, S.V.; Firsov, A.A. Two-dimensional gas of massless Dirac fermions in graphene. *Nature* **2005**, *438*, 197.
2. Zhang, Y.; Tan, Y.W.; Stormer, H.; Kim, P. Experimental observation of the quantum Hall effect and Berry's phase in graphene. *Nature* **2005**, *438*, 201.
3. Chen, C.F.; Park, C.H.; Boudouris, B.W.; Horng, J.; Geng, B.; Girit, C.; Zettl, A.; Crommie, M.F.; Segalman, R.A.; Louie, S.G.; Wang, F. Controlling inelastic light scattering quantum pathways in graphene. *Nature* **2011**, *471*, 617.
4. Ando, T.; Nakanishi, T.; Saito, R. Berry's Phase and Absence of Back Scattering in Carbon Nanotubes. *J. Phys. Soc. Jpn.* **1998**, *67*, 2857.
5. Tuinstra, F.; Koenig, J.L. Raman Spectrum of Graphite. *J. Chem. Phys.* **1970**, *53*, 1126–1130.
6. Katagiri, G.; Ishida, H.; Ishitani, A. Raman spectra of graphite edge planes. *Carbon* **1988**, *26*, 565 – 571.
7. Cançado, L.G.; Pimenta, M.A.; Neves, B.R.A.; Dantas, M.S.S.; Jorio, A. Influence of the Atomic Structure on the Raman Spectra of Graphite Edges. *Phys. Rev. Lett.* **2004**, *93*, 247401.
8. You, Y.; Ni, Z.; Yu, T.; Shen, Z. Edge chirality determination of graphene by Raman spectroscopy. *Appl. Phys. Lett.* **2008**, *93*, 163112.
9. Gupta, A.K.; Russin, T.J.; Gutierrez, H.R.; Eklund, P.C. Probing Graphene Edges via Raman Scattering. *ACS Nano* **2009**, *3*, 45–52.

10. Cong, C.; Yu, T.; Wang, H. Raman Study on the G Mode of Graphene for Determination of Edge Orientation. *ACS Nano* **2010**, *4*, 3175–3180.
11. Thomsen, C.; Reich, S. Double Resonant Raman Scattering in Graphite. *Phys. Rev. Lett.* **2000**, *85*, 5214–5217.
12. Sasaki, K.; Kato, K.; Tokura, Y.; Suzuki, S.; Sogawa, T. Pseudospin for Raman D band in armchair graphene nanoribbons. *Phys. Rev. B* **2012**, *85*, 075437.
13. Wallace, P.R. The Band Theory of Graphite. *Phys. Rev.* **1947**, *71*, 622–634.
14. Slonczewski, J.C.; Weiss, P.R. Band Structure of Graphite. *Phys. Rev.* **1958**, *109*, 272–279.
15. Sakurai, J. *Advanced Quantum Mechanics*; Addison-Wesley: Canada, 1967.
16. Baranov, A.V.; Bekhterev, A.N.; Bobovich, Y.S.; Petrov, V.I. Interpretation of certain characteristics in Raman spectra of graphite and glassy carbon. *Optics and Spectroscopy* **1987**, *62*, 612–616.
17. Pócsik, I.; Hundhausen, M.; Koós, M.; Ley, L. Origin of the D peak in the Raman spectrum of microcrystalline graphite. *Journal of Non-Crystalline Solids* **1998**, *227230, Part 2*, 1083 – 1086.
18. Sasaki, K.; Saito, R. Pseudospin and Deformation-Induced Gauge Field in Graphene. *Prog. Theor. Phys. Suppl.* **2008**, *176*, 253–278.
19. Sasaki, K.; Wakabayashi, K.; Enoki, T. Electron Wave Function in Armchair Graphene Nanoribbons. *J. Phys. Soc. Jpn.* **2011**, *80*, 044710.
20. Sasaki, K.; Saito, R.; Wakabayashi, K.; Enoki, T. Identifying the Orientation of Edge of Graphene using G Band Raman Spectra. *J. Phys. Soc. Jpn.* **2010**, *79*, 044603.
21. Maeta, H.; Sato, Y. Raman spectra of neutron-irradiated pyrolytic graphite. *Solid State Commun.* **1977**, *23*, 23 – 25.
22. Nemanich, R.J.; Solin, S.A. First- and second-order Raman scattering from finite-size crystals of graphite. *Phys. Rev. B* **1979**, *20*, 392–401.
23. Grüneis, A.; Saito, R.; Samsonidze, G.G.; Kimura, T.; Pimenta, M.A.; Jorio, A.; Filho, A.G.S.; Dresselhaus, G.; Dresselhaus, M.S. Inhomogeneous optical absorption around the K point in graphite and carbon nanotubes. *Phys. Rev. B* **2003**, *67*, 165402.
24. Sasaki, K.; Kato, K.; Tokura, Y.; Oguri, K.; Sogawa, T. Theory of optical transitions in graphene nanoribbons. *Phys. Rev. B* **2011**, *84*, 085458.
25. Vidano, R.; Fischbach, D.; Willis, L.; Loehr, T. Observation of Raman band shifting with excitation wavelength for carbons and graphites. *Solid State Commun.* **1981**, *39*, 341 – 344.
26. Matthews, M.J.; Pimenta, M.A.; Dresselhaus, G.; Dresselhaus, M.S.; Endo, M. Origin of dispersive effects of the Raman D band in carbon materials. *Phys. Rev. B* **1999**, *59*, R6585–R6588.
27. Casiraghi, C.; Hartschuh, A.; Qian, H.; Piscanec, S.; Georgi, C.; Fasoli, A.; Novoselov, K.S.; Basko, D.M.; Ferrari, A.C. Raman Spectroscopy of Graphene Edges. *Nano Lett.* **2009**, *9*, 1433.
28. Sasaki, K.i.; Kato, K.; Tokura, Y.; Suzuki, S.; Sogawa, T. Decay and frequency shift of both intervalley and intravalley phonons in graphene: Dirac-cone migration. *Phys. Rev. B* **2012**, *86*, 201403.
29. Piscanec, S.; Lazzeri, M.; Mauri, F.; Ferrari, A.C.; Robertson, J. Kohn Anomalies and Electron-Phonon Interactions in Graphite. *Phys. Rev. Lett.* **2004**, *93*, 185503.

30. Begliarbekov, M.; Sul, O.; Kalliakos, S.; Yang, E.H.; Strauf, S. Determination of edge purity in bilayer graphene using mu-Raman spectroscopy. *Appl. Phys. Lett.* **2010**, *97*, 031908.
31. Zhang, W.; Li, L.J. Observation of Phonon Anomaly at the Armchair Edge of Single-Layer Graphene in Air. *ACS Nano* **2011**, *5*, 3347–3353.
32. Fujita, M.; Igami, M.; Nakada, K. Lattice Distortion in Nanographite Ribbons. *Journal of the Physical Society of Japan* **1997**, *66*, 1864–1867.
33. Son, Y.W.; Cohen, M.L.; Louie, S.G. Energy Gaps in Graphene Nanoribbons. *Phys. Rev. Lett.* **2006**, *97*, 216803.
34. Sasaki, K.; Wakabayashi, K. Chiral gauge theory for the graphene edge. *Phys. Rev. B* **2010**, *82*, 035421.
35. Begliarbekov, M.; Sasaki, K.I.; Sul, O.; Yang, E.H.; Strauf, S. Optical Control of Edge Chirality in Graphene. *Nano Letters* **2011**, *11*, 4874–4878.